Modeling and experimental validation of microstructure and mechanical properties of ductile iron during solidification

Jianzheng Guo and Mark T. Samonds
ESI US R&D, 5850 Waterloo Road, Suite 140, Columbia, MD, 21045

Abstract

Ductile irons are still important engineering materials due to their high strength and toughness, and relatively low price. In foundries, ductile irons suffer from shrinkage porosity formation during solidification, which is detrimental to their mechanical properties. In order to minimize porosity formation, large risers are normally used in the design, which reduces porosity level sometimes but leads to a low yield. In order to better understand the shrinkage behavior of ductile iron during solidification, a micro model was developed to simulate the microstructure formation. The density change during solidification and the room temperature mechanical properties can be calculated based on the microstructure. The simulation has been compared with experimental results and found to be in good agreement.

Keywords: Solidification modeling, solidification microstructure, mechanical properties, ductile cast iron.

1. Introduction

Cast iron remains the most important casting material with over 70% of the total world tonnage [1]. Based on the shape of graphite, cast iron can be lamellar (flake) graphite iron or spheroidal (nodular) graphite iron. In the last forty years, many papers have been published on the modeling of ductile iron solidification. It started with computational modeling by analytical heat transport and transformation kinetics calculations [2–8]. The computer model can calculate the cooling curve with an analytical method, together with the kinetics calculation of carbon diffusion through the gamma phase shell. In 1985, Su *et al.* [9] first coupled heat transfer and solidification kinetics in a model using the finite difference method. After that, many papers have been published on micro modeling of ductile iron solidification [10–20]. Carbon diffusion controlled growth through the gamma shell was treated. In those models, the nodule count, graphite radius, and austenite shell radius were calculated. Onsoien *et al.* [21,22] used an internal state variable approach to model the multiple phase changes occurring during solidification and subsequent cooling of near eutectic ductile cast iron. In their simulation, the effects on the microstructure evolution at various stages of the process arising from alloy composition, graphite nucleation potential, and thermal progress were illuminated. Heat flow, fading effect, graphite/austenite eutectic transformation, ledeburite eutectic transformation, graphite growth in the austenite regime, and the eutectoid transformation were all modeled. In this paper, a comprehensive micro model is developed which can give accurate microstructural information as well as the mechanical properties, such as yield strength, tensile strength, and hardness. The fractions of austenite, ferrite, pearlite, graphite, liquid, and ledeburite are all calculated. The prediction has been compared with experimental results and found to be in good agreement.

2. Micro modeling

2.1 Nucleation model

In this work, Oldfield's nucleation model [2] is applied. Bulk heterogeneous nucleation occurs at foreign sites which are already present within melt or intentionally added to the melt by inoculation.

$$N_o = A(\Delta T)^n \tag{1}$$

where A is the nucleation constant, N_o is the nucleation number per unit volume, ΔT is the undercooling, and n is another constant which depends on the effectiveness of inoculation.

2.2 Fading effect

Fading is the phenomenon whereby the effectiveness of inoculation diminishes as the time between inoculation and casting increases. It is believed that the nucleation of graphite occurs on small nonmetallic inclusions which are entrapped in the liquid after inoculation [18]. The small particles will grow with time. The particle diameter can be calculated from:

$$d = (d_o^3 + kt)^{1/3} \tag{2}$$

where d is the particle diameter at time t, d_o is the particle diameter at the beginning of inoculation, and k is a kinetic constant.

2.3 Graphite/austenite eutectic transformation

The eutectic growth process in ductile iron is a divorced growth of austenite and graphite, which do not grow concomitantly. At the beginning of the liquid/solid transformation, graphite nodules nucleate in the liquid and grow in the liquid to a small extent. The formation of graphite nodules and their limited growth in the liquid depletes carbon in the melt in the vicinity of the nodules. This facilitates the nucleation of austenite around the nodules, forming a shell. Further growth of these nodules is by diffusion of carbon from the melt through the austenite shell. Once the austenite shell is formed around each nodule, the diffusion equation for carbon through the austenitic shell is solved in 1-D spherical coordinates. The boundary conditions are known from the phase diagram because thermodynamic equilibrium is maintained locally. Conservation of mass and solute is maintained in each grain. Because of the density variation resulting from the growth of austenite and graphite, expansion/contraction of the grain is taken into account by allowing the final grain size to vary. Toward the end of solidification, the grains impinge on each other. This is taken into consideration by using the Johnson-Mehl approximation.

Using spherical coordinates, a mass balance is written as:

$$\rho_G \frac{4}{3}\pi R_G^3 + \rho_\gamma \frac{4}{3}\pi (R_\gamma^3 - R_G^3) + \rho_l \frac{4}{3}\pi (R_l^3 - R_\gamma^3) = m_{av} \quad (3)$$

where ρ_G, ρ_γ, ρ_l are the densities of graphite, austenite, and liquid respectively and the calculation can be found in the next section; R_G, R_γ, R_l are radii of graphite, austenite, and of the final grain, respectively; m_{av} is the average mass of the grain.

Assuming complete mixing of solute in the liquid, the overall solute balance is written as:

$$\rho_G \cdot 1 \cdot \frac{4}{3}\pi R_G^3 + \int_{R_c}^{R_a} \rho_\gamma c(r,t) 4\pi r^2 dr + \rho_l c_l \frac{4}{3}\pi (R_l^3 - R_\gamma^3) = c_{av} \quad (4)$$

Differentiation of the above two equations and using Fick's law in spherical coordinates leads to two equations for graphite and austenite growth rates following some manipulation.

2.4 Ledeburite eutectic transformation

When the temperature reaches below the metastable eutectic temperature, the metastable eutectic phase forms. The metastable cementite eutectic is also called ledeburite, in which small islands of austenite are dispersed in the carbide phase. It has both direct and indirect effects on the properties of ductile iron castings. It increases the yield strength

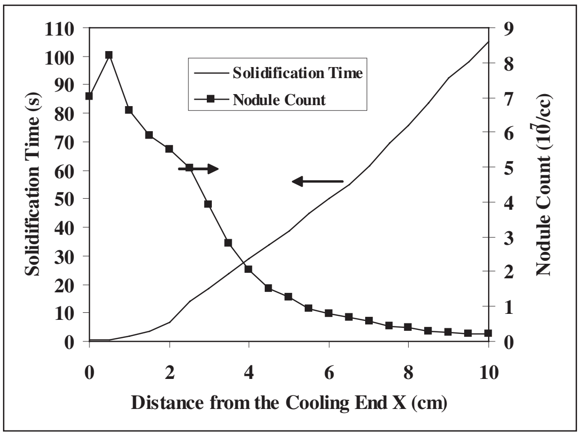

Figure 1: Solidification time and nodule count at different distances from the chill.

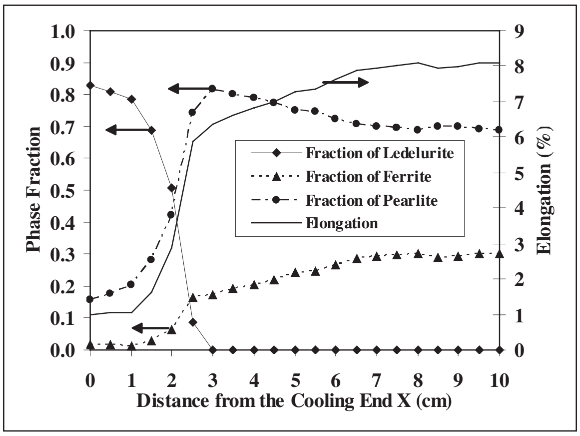

Figure 2: Phase fractions and elongation to fracture of the casting at different distances from the chill.

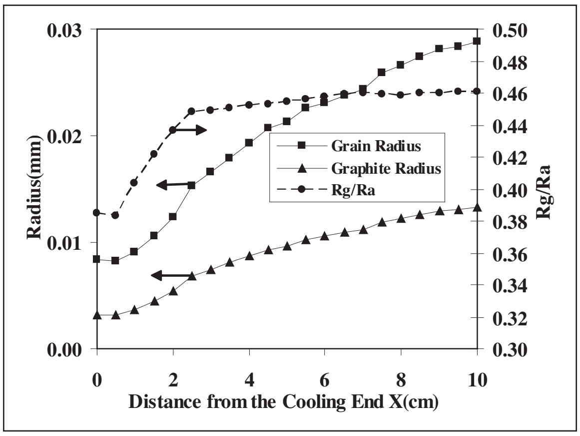

Figure 3: Grain and graphite size in the casting at different distances from the chill.

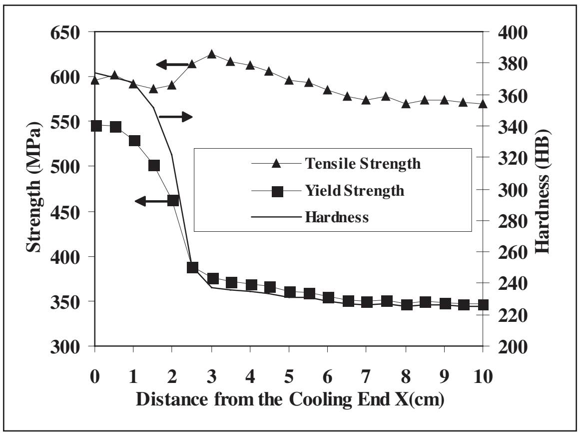

Figure 4: Mechanical properties of the casting at different distances from the chill.

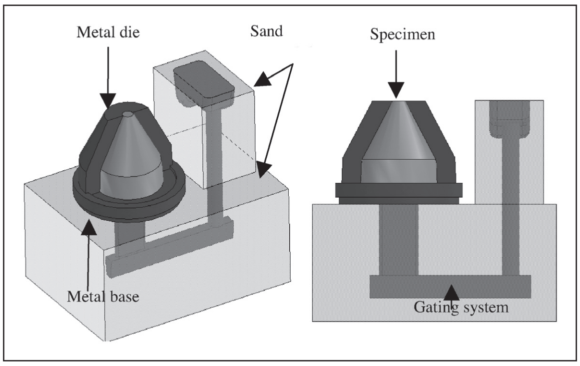

Figure 5: Experimental set-up.

but reduces the tensile strength with an increasing volume percent of the hard, brittle carbide. Following the assumptions from Onsoien *et al.* [22], the graphite/austenite nodule distribution is approximated by that of a close-packed face-centered space lattice and the ledeburite eutectic appears in intermediate positions. The total number of ledeburite nucleation sites is the same as that of graphite/austenite nodules. Each grain is assumed to be spherical. Hence the growth of the ledeburite can be calculated as:

$$\frac{dR_{LE}}{dt} = 30.0 \cdot 10^{-6} * (\Delta T)^n \quad (5)$$

So the fraction of ledeburite can be written as:

$$f_{LE} = \frac{4}{3}\pi N R_{LE}^3 \quad (6)$$

2.5 Eutectoid transformation

The eutectoid reaction leads to the decomposition of austenite to ferrite and graphite for the case of the stable eutectoid, and to pearlite for the metastable eutectoid transformation. Usually, the metastable eutectoid temperature is lower than the stable eutectoid temperature. Slower cooling results in the more stable eutectoid structure. Following solidification, the solubility of carbon in austenite decreases with the drop in temperature until the stable eutectoid temperature is reached. The rejected carbon migrates towards the graphite nodules, which are the carbon sinks. This results in carbon depleted regions in austenite around the graphite nodules. This provides favorable sites for ferrite to nucleate, which grow as a shell around the graphite nodules. If the complete transformation of austenite is not achieved when the metastable temperature is reached, pearlite forms and grows in competition with ferrite.

3. Mechanical properties calculation

The ultimate goal of process modeling is to predict the final mechanical properties. The mechanical properties (hardness, tensile strength, yield strength, and elongation) of ductile iron castings are functions of composition and microstructure. The graphite shape, graphite structure, graphite amount, carbide content, and matrix structure (pearlite, ferrite) all affect the mechanical properties of ductile iron castings. Carbide content has direct and indirect effects on the properties of cast ductile irons. The hard brittle carbide increases the yield strength but decreases the tensile strength. As for the matrix structure, increasing the amount of pearlite increases strength and hardness but reduces the elongation.

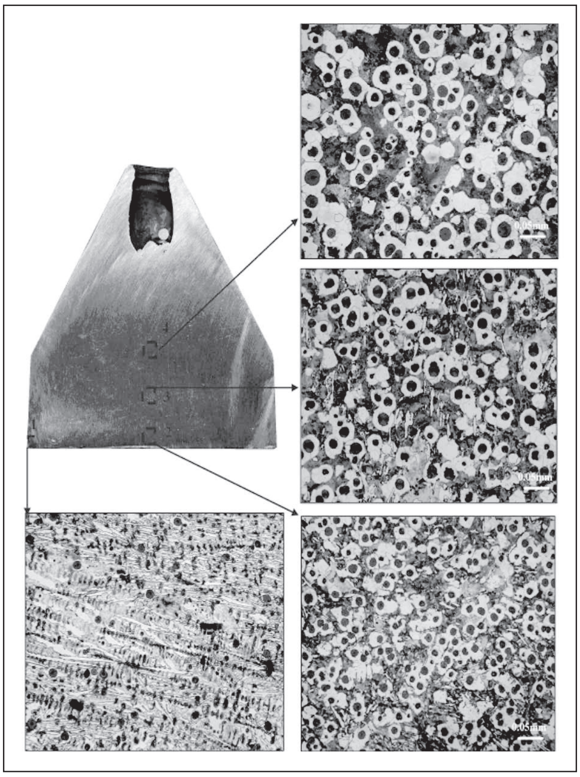

Figure 6: Microstructure of ductile iron at indicated points.

4. Case studies

In order to show the capability of this model, solidification in a simple geometry ductile iron casting was investigated. The dimensions of the casting are 10 × 10 × 200 cm. On the left face, it is cooled by contacting a constant temperature media (15°C) with a heat transfer coefficient of 500 W/m^{2}K. All the other faces are adiabatic. The initial melt temperature is 1400°C. Figure 1 shows the solidification time for different distances from the cooling end. At the very left, the solidification time is less than 1 second. On the other hand, the solidification time at 10 cm from the cooling end is more than 100 seconds. Because of the different cooling rates, the nodule count varies and is shown in the same Figure. The metastable phase forms when cooling is too fast. Figure 2 shows the volume fraction of different phases at room temperature. On the very left end, there is around 90% volume fraction of ledeburite. It reduces gradually from left to right until at 3 cm from the chill end, there is no ledeburite. At the same time, as cooling decreases, the volume fraction of ferrite increases and that of pearlite decreases. Ledeburite is a very hard, brittle phase, harder than pearlite. Pearlite is harder than ferrite. Hence ductility increases as the cooling rate decreases. From the micro modeling, the calculated grain and graphite radii at different distances from the chill are shown in Figure 3. Faster cooling results in smaller grain and graphite sizes. The ratio of the radius of graphite and austenite increases as cooling decreases, but reaches a constant value of around

0.46 even though the radius of graphite and austenite still continue to increase. This constant ratio is determined by the initial carbon content. It can determine the expansion level during solidification.

Based on the microstructure, the mechanical properties can be calculated. As mentioned above, carbide increases yield strength but decreases tensile strength. The yield strength and hardness continuously decrease as the cooling rate decreases. The yield strength is very high on the left because of the formation of carbide. The results are shown in Figure 4.

5. Experimental validations

In order to validate the model, a series of experiments was performed [23]. A three-part cast-iron foundry mould containing the gating system is shown in Figure 5. The casting is GGG60 ductile iron. The pouring temperature is 1400°C, the initial die temperature is 165°C, and the initial sand temperature is 20°C. In order to investigate the structure of the casting and the morphology of graphite, specimens were taken as shown in Figure 6. The specimens were then ground, polished, and etched for structure evaluation. It can be seen in the photomicrographs that graphite was segregated in the form of spheroids.

Because of the rapid cooling, a large amount of metastable ledeburite was formed in the corners. The ledeburite reduces gradually as the cooling rate decreases. In the center of the casting, no ledeburite was found. The radius of the black graphite balls increases as cooling decreases. The structure of the metal is formed with pearlite and ferrite. Figure 7 shows the volume fraction of metastable phase (top) and volume fraction of ferrite (bottom). It is difficult to measure the yield strength of the sample at different locations because the strength could change dramatically based on microstructure variation. On the other hand, hardness is an excellent indicator of strength and relatively easy to measure. Figure 8 shows the hardness measurement points on the sample. Table 1 shows a comparison between measurement and prediction for hardness at different locations. It can be concluded that the prediction matches the experiments very well.

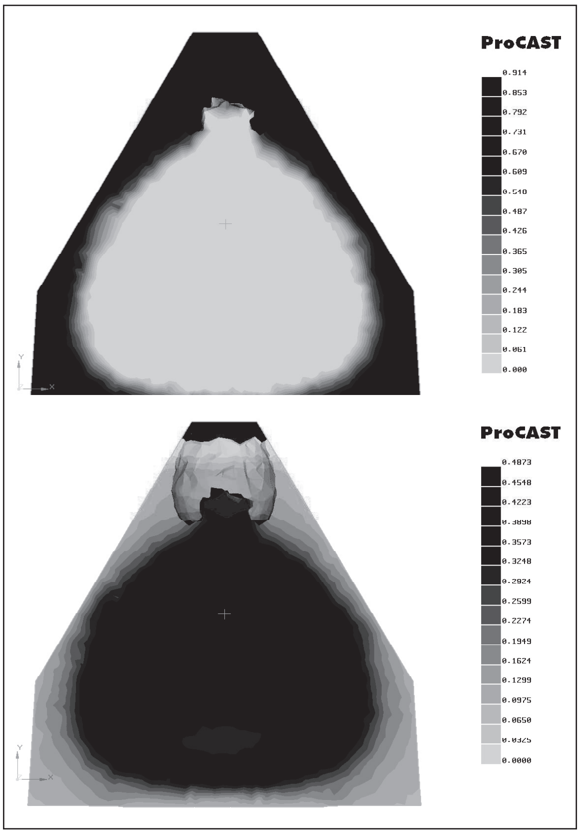

Figure 7: Simulation results of fraction of metastable phase (top) and fraction of ferrite (bottom).

6. Conclusions

A micro model has been developed to simulate microstructure formation of ductile iron. The density change during solidification and the room temperature mechanical properties can be calculated based on the microstructure. The simulation has been compared with experimental results and found to be in good agreement.

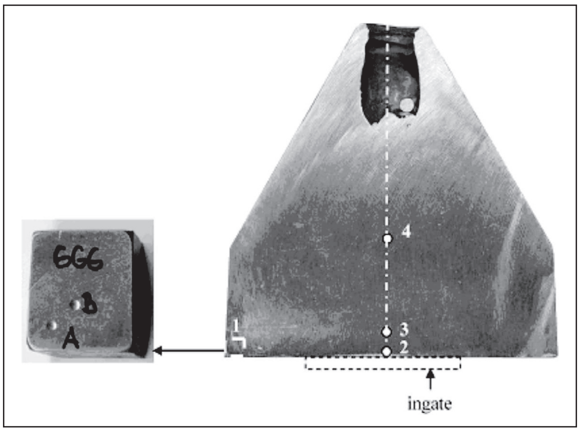

Figure 8: Sample for hardness measurement.

Table 1: Comparison between measured and predicted hardness.

Location	Dimension x [mm]	Dimension y [mm]	Measurement HB	Simulated HB
1 A	4	4	368	371
B	10	7	313	320
2	50	4	249	255
3	50	10	236	245
4	50	48	209	203

References

1. D.M. Stefanescu, Mater. Sci. Eng. A, **A413–414** (2005) 322–333.
2. W. Oldfield, ASM Trans., **59** (1966) 945.
3. D.M. Stefanescu, S. Trufinescu, Z. Metallkunde, **9** (1974) 610.
4. H. Fredriksson, L. Svensson, in: H. Fredriksson, M. Hillert (Eds.), The Physical Metallurgy of Cast Iron, Elsevier, 1985, pp. 273–284.
5. H. Fredriksson, L. Svensson, in: D.M. Stefanescu, G.J. Abbaschian, R.J. Bayuzick (Eds.), Solidification Processing of Eutectic Alloys, The Metallurgical Soc., Warrendale, PA, 1988, pp. 153–162.
6. D.M. Stefanescu, C. Kanetkar, in: D.J. Srolovitz (Ed.), Computer Simulation of Microstructural Evolution, The Metallurgical Soc., Warrendale, PA, 1985, pp. 171–188.
7. J. Lacaze, M. Castro, C. Selig, G. Lesoult, in: M. Rappaz, *et al*. (Eds.), Modeling of Casting, Welding and Advanced Solidification Processes V, The Metallurgical Soc., Warrendale, PA, 1991, pp. 473–478.
8. E. Fras, W. Kapturkiewicz, A.A. Burbielko, in: M. Croos, J. Campbell (Eds.), Modeling of Casting, Welding and Advanced Solidification Processes VII, The Metallurgical Soc., Warrendale, PA, 1995, pp. 679–686.
9. K.C. Su, I. Ohnaka, I. Yamauchhi, T. Fukusako, in: H. Fredriksson, M. Hillert (Eds.), The Physical Metallurgy of Cast Iron, Elsevier, 1985, pp. 181–189.
10. S. Chang, D. Shangguan, D.M. Stefanescu, Metall. Trans. A, **22A** (1991) 915.
11. D.M. Stefanescu and C.S. Kanetkar, AFS Trans., **95** (1987) 139–144.
12. L. Nastac and D.M. Stefanescu, AFS Trans., **103** (1995) 329–337.
13. D.M. Stefanescu, A. Catalina, X. Guo, L. Chuzhoy, M.A. Pershing, and G.L. Biltgen, in: Solidification Processing 1997, Edited by J. Beech and H. Jones, 7–9 July 1997, University of Sheffield, UK, pp. 609–613.
14. G. Lesoult, M. Castro, and J. Lacaze, Acta Mater., **46** (1998) 983–995.
15. G. Lesoult, M. Castro, and J. Lacaze, Acta Mater., **46** (1998) 997–1010.
16. F.J. Bradley, Metall. Trans. B., **24B**, 539 (1990).
17. R. Vijayaraghavan and F.J. Bradley, Scripta Mater., **41** (1999) 1247–1253.
18. D. Venugopalan, Metall. Trans. A, 1990, **21A**, 913–918.
19. L. Nastac and D.M. Stefanescu, AFS Trans., 1995, **103**, 329–337.
20. Q. Chen, E.W. Langer, and P.N. Hansen: Scand. J. Metall., 1995, **24**, 48–62.
21. M.I. Onsoien, O. Grong, O. Gundersen, and T. Skaland, Metall. Mater. Trans. A, **30A** (1999) 1053–1068.
22. M.I. Onsoien, O. Grong, O. Gundersen, and T. Skaland, Metall. Mater. Trans. A, **30A** (1999) 1069–1079.
23. Vladimír Krutiš and Jaromír Roučka, Shrinkage of Graphitic Cast Irons, ESI Group Internal Report. ■